



A Study on YSZ Abradable Seal Coatings Prepared by Atmospheric Plasma Spray and Mixed Solution Precursor Plasma Spray

Xiaoming Sun^{1,2,3} · Zhiang Liu⁴ · Lingzhong Du^{1,2} · Hao Lan^{1,2} · Huifeng Zhang¹ · Chuanbing Huang¹ · Maoqiao Xiang¹ · Fen Yue¹ · Weigang Zhang^{1,3}

Submitted: 30 November 2020 / in revised form: 1 February 2021 / Accepted: 2 February 2021 / Published online: 11 April 2021
© ASM International 2021

Abstract The yttria-stabilized zirconia (YSZ) ceramic has been proved to be a promising material for abradable seal coatings. In this research, abradable seal coatings named C-YSZ and M-YSZ were prepared by applying the conventional plasma spraying method with improved nanostructured powders and by the mixed solution precursor plasma spraying technique, respectively. A study on the microstructure, mechanical properties, oxidation resistance and hot corrosion resistance was conducted on both C-YSZ and M-YSZ coatings by using scanning electron microscopy, transmission electron microscopy, muffle furnace and x-ray diffractometer. The results show that the C-YSZ coating presents larger-size pores with denser YSZ structures and grains showing size larger than 100 nm distributed around the pores compared with M-YSZ, in which the pores are much smaller and the grain size is 20–30 nm. As a result, the M-YSZ coating displays lower hardness and bond strength compared with C-YSZ. The oxidation tests show that the M-YSZ coating possesses better

oxidation resistance due to the nanostructure topcoat compared with C-YSZ. However, the hot corrosion tests indicate that both the C-YSZ coating and the M-YSZ coating fail to present ideal hot corrosion resistance.

Keywords abradable seal coatings · hot corrosion behavior · microstructure · oxidation resistance · Yttria-stabilized zirconia

Introduction

Abradable seal coatings have been used in low- and high-pressure sections of jet engine compressors for more than 50 years. Today, abradable seal coatings are widely applied in the field of aeroengines to reduce the clearance between the applied coatings and rotating blades for improving the compressor efficiency and reducing fuel consumption (Ref 1–3). Aside from being abradable, this kind of coating is usually desired to be mechanically stable and withstand high thermomechanical loadings. So far, many research works have been devoted to increasing the life time and durability of abradable seal coatings during service. Specifically, applying abradable seal coatings based on yttria-stabilized zirconia (YSZ) has drawn much attention in the research field of thermal spray industry. Foroushani et al. studied the high-temperature oxidation behavior, porosity and microstructure of different YSZ abradable seal coatings and found that volume percentage of porosity in the YSZ coatings containing LaPO₄ was higher than that of the monolithic YSZ coatings (Ref 4). Ding et al. investigated the formation and properties of porous YSZ coatings by using poly-p-hydroxybenzoate (PHB) powder mixed with the YSZ powder as pore-forming material (Ref 5). Ebert et al. studied an atmospheric plasma-sprayed ceramic double-layer abradable seal

✉ Weigang Zhang
wgzhang@ipe.ac.cn

Lingzhong Du
lzdu@ipe.ac.cn

¹ State Key Laboratory of Multiphase Complex Systems, Key laboratory of Science and Technology on Particle Materials, Institute of Process Engineering, Chinese Academy of Sciences, Beijing 100190, China

² Innovation Academy for Green Manufacture, Chinese Academy of Sciences, Beijing 100190, China

³ University of Chinese Academy of Sciences, Beijing 100049, China

⁴ Experimental Teaching and Equipment Management Center, Qufu Normal University, Shandong 273165, China

coating system composed of YSZ as an intermediate layer and magnesia alumina spinel as a top layer, and the results showed that the coatings presented a typical failure mechanism with exfoliation of thin coating lamellae starting from the coating surface after thermal cycles (Ref 6). It is reported that YSZ as abradable seal coatings can advantageously combine a suitable thermal conductivity with a relatively high thermal expansion coefficient, but display a high-temperature capability limitation in long-term applications (Ref 7). As a result, increasing efforts are devoted to developing YSZ-based abradable seal coatings with excellent properties, especially under relatively high temperature conditions.

Nowadays, the serve conditions of aeroengines are getting more and more complicated and rigorous, and traditional YSZ coatings may face difficulties in meeting many of the rising performance requirements such as high-temperature oxidation resistance, excellent hot corrosion resistance, and so on (Ref 8–10). Significantly, for the YSZ-based coatings the spallation of ceramic coatings from bond coat can occur during thermal cycles or high-temperature oxidation process (Ref 11, 12) when the thermal-grown oxide (TGO) layer at the interface of ceramic layer and bond coat is formed by O₂ diffusion from top ceramic layer and the oxidation at the interface, and phase transformation and spallation of surface layers can be formed by the diffusion of corrosive salts such as V₂O₅. To address these challenges, scientists started to plunge into the preparation of YSZ-based coatings with nanostructures, and it is reported that the plasma spraying of nanostructured powders is an effective mean to obtain nanostructured coatings (Ref 13–16). In our previous work, we prepared the YSZ abradable seal coatings through mixed solution precursor plasma spraying method (M-YSZ) and studied its microstructure and mechanical properties (Ref 17). Preliminary studies have shown that the coatings obtained by mixed solution precursor plasma spraying method display high porosity of nanostructure. Hence, in this work we further prepared YSZ abradable seal coatings by applying the conventional atmospheric plasma spray method with improved nanostructured YSZ powders (C-YSZ). A study of the microstructure and mechanical properties was conducted between the C-YSZ and M-YSZ coatings. Moreover, the stability of C-YSZ coating and the related analysis from the microstructure point of view were compared to the particulate M-YSZ coating by means of high-temperature oxidation and hot corrosion test. This work may shed light on the design of nanostructured abradable seal coatings with improved high-temperature properties.

Experimental

Feedstock and Coating Preparation

The coating named M-YSZ was prepared by using plasma spraying method with a blend of YSZ nanoparticles and

YSZ solution precursor. 20% mass fraction of solution precursor YSZ system with the molar ratio Y:Zr of 8:92 was obtained by dissolving zirconium nitrate (shown in Fig. 1a) and yttrium nitrate (shown in Fig. 1b) in a mixture of 1.5 L deionized water and 0.3 L absolute ethyl alcohol at 50 °C. After that, a mixed slurry with 5 g YSZ nanoparticles (shown in Fig. 1c) and polyacrylic acid was well mixed into the above solution precursor with the YSZ mass fraction of 20% for the final mixed solution precursor (Ref 18). The conventional YSZ abradable seal coating named C-YSZ was prepared by plasma spraying of a blend of YSZ particles, polyphenylene ester and water glass binder (40% diluted with water). The YSZ particles were first fully mixed with 4% water glass binder (mass fraction), and then the mixture was thoroughly added with PHB of 6% (mass fraction). The mixture was packed down hard, dried at 80 °C for 30 min, dispersed and finally passed between a 100-mesh and 320-mesh sieve to obtain the final pore-forming powders (shown in Fig. 1d). The Ni-based superalloy plates with the composition of 74Ni-20Cr-2.6Ti-0.8Al-2.6Fe (GH4033) with the size of $\Phi 25 \times 5 \text{ mm}^3$ were used as the substrates after the grit blasting process. The powders named CoNiCrAlY with the composition of 37Co-31.5Ni-25.5Cr-5.5Al-0.5Y were used as the bonding layers to strengthen the bond strength between the substrates and coatings. The bonding layers and the coatings were both deposited by APS-2000K plasma spray system, and the respective schematic diagrams for obtaining the M-YSZ and C-YSZ coatings are shown in Fig. 2. The C-YSZ coating prepared by plasma spraying was then heated to 650 °C and kept for 2 h in the open atmosphere to burn polyester out after the plasma spray process. The parameters of the spraying processes for both methods are shown in Table 1.

Microstructural Characterization

The scanning electron microscopy (SEM, JSM-7001F, Japan) with an energy-dispersive spectroscopy (EDS) system was applied on the observations of microstructures on both C-YSZ and M-YSZ coatings. By further applying transmission electron microscopy (TEM, JEM-2100F, Japan) and high-resolution transmission electron microscopy (HRTEM), the nanostructure morphologies of both coatings were characterized. The phase compositions of the coatings were identified on a x-ray diffractometer (XRD, PANalytical B.V., X'Pert Pro MPD, Holland, Cu K α , $\lambda = 1.5418 \text{ \AA}$), with the angular ranges of 5°–90°. The Image Pro Plus 6.0 (Ref 19) was used to calculate the porosity of the coatings by applying five cross-section images at $\times 5000$ magnification on all the samples, where the pores were identified by using image thresholding.

Fig. 1 SEM images of powders: (a) $Zr(NO_3)_4$, (b) $Y(NO_3)_3$, (c) YSZ and (d) improved YSZ

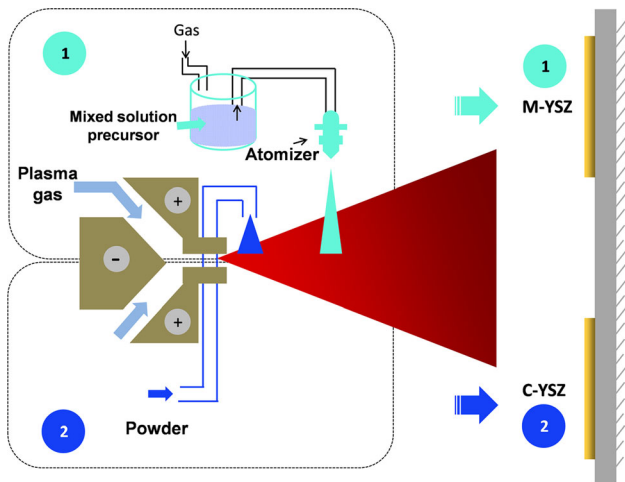
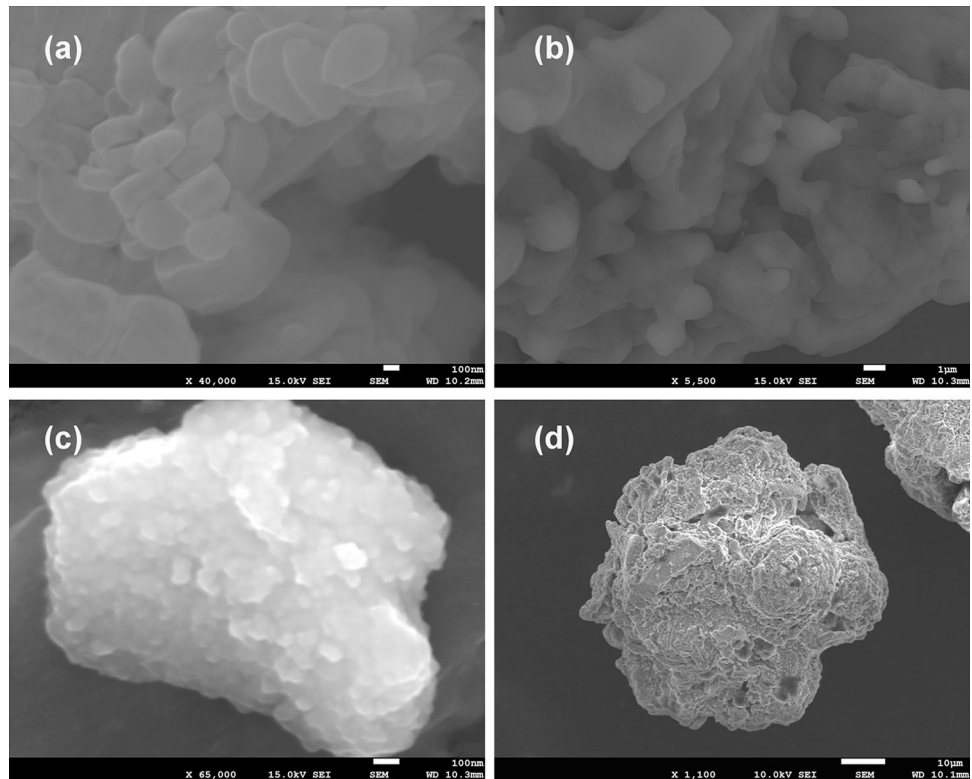


Fig. 2 Schematic diagram of preparation methods for YSZ abrasible seal coatings by atmospheric plasma spray and mixed solution precursor plasma spray

Oxidation Resistance Tests

Oxidation resistance tests were carried out at 1150 °C, and both the M-YSZ and the C-YSZ coatings were held for intervals of 4, 12, 48, 100 and 120 h at this temperature. After that, the samples were cut into pieces and polished before the observation by SEM. The thicknesses of the TGO layer formed between ceramic and bond coat were taken as an evaluation of high-temperature oxidation

resistance of coatings. For the C-YSZ and M-YSZ coatings, the TGO layer thickness was determined by taking from the average value of three different parts, respectively.

Hot Corrosion Tests

Hot corrosion tests were done at 900 °C in the present work and performed by brushing the powder mixture of 60 wt.% V_2O_5 and 40 wt.% Na_2SO_4 on the surfaces of coatings uniformly (leaving approximately 2 mm from the edge to avoid edge effect) and then heating them in the furnace under air condition to 900 °C. After specific intervals of 4, 12, 24, 48, 96 and 120 h, the furnace was switched off and all the samples were withdrawn from it at room temperature.

Mechanical Properties

A HSRS-45 surface hardness tester (HuaYin Tester, China) was used to test the surface Rockwell HR15Y hardness of all the coatings. An average of ten measurements on the samples was taken as the final hardness value.

The universal material testing machine controlled by a commercial WDW-100E microcomputer and the performing standard referenced by ASTM C633-2013 with a speed of 0.1 mm/min were used to test the bond strength of all the samples. Both the surfaces of two bond rods and the back

Table 1 Parameters of plasma spraying process for C-YSZ and M-YSZ

Items	C-YSZ	M-YSZ
Current (A)	600	510
Voltage (V)	60	60
Spraying distance (mm)	120	55
Ar flow rate (L/min)	35	40
H ₂ flow rate (L/min)	10	1.8
Liquid flow rate (L/min)	...	0.012
Powder feeding rate (g/min)	20	...
Atomizing gas pressure (MPa)	...	0.4
Axial distance from jet to atomizing nozzle (mm)	...	10
Vertical distance from jet to atomizing nozzle (mm)	...	20

of the coating sample were firstly sandblasted, and then some No.914 super was taken to bond the surface and the back of the coatings to the bond rods, respectively. After that, all the samples were vertically taken into a drying oven at 80 °C for 4 h. The bond strengths of both coatings were calculated by the following equation:

$$F = G/S \quad (\text{Eq 1})$$

where G (N) is the loading when breaking, and S (m²) is the total effective coating area.

Results and Discussion

Microstructure of YSZ Coatings

Figure 3(a) and (b) shows the macrosurface morphologies of C-YSZ and M-YSZ abrasible seal coatings, respectively. Some microscopic pores can be seen on the surface of C-YSZ, while these pores cannot be detected on the surface of M-YSZ and instead some microscopic spherical protrusions are present on the M-YSZ coatings' surface. Figure 3(c) and (d) shows the enlarged views of surface morphologies of the C-YSZ and M-YSZ coatings shown in Fig. 3(a) and (b). On the surface of C-YSZ, it seems that a stack of YSZ powders from the molten state distributes closely around the micron pores; the pores are larger than 10 μm in average from Fig. 3(c). This is common in thermal-sprayed coatings with pores where splats are located around pores after the spraying process. However, for the M-YSZ abrasible seal coating, the surface is like the stack of a mixture of melted nanosized YSZ powders and unmelted nanopowders (Fig. 3d), with pores of submicron size or nanoscale unevenly distributed, and the pores seem smaller than 1 μm in average. Figure 4(a) presents the SEM image of the cross section of the C-YSZ abrasible seal coating, which presents the bond coat and a porous microstructure with large-sized pores in the YSZ ceramic layer.

Figure 4(b) shows the SEM image of the cross section of nanostructured M-YSZ abrasible seal coating, which shows the layers of bond coat and different sizes of porous microstructure in the YSZ ceramic coating. In Fig. 4(b), the number of large-sized pores in M-YSZ is much less than that of the C-YSZ coating in Fig. 4(a), and the average size of the existing pores is much smaller. Based on the observed porous structures, our careful calculation shows that the porosities of the C-YSZ- and M-YSZ-deposited abrasible seal coatings are 33.7% and 30.4%, respectively.

Figure 5 displays the x-ray diffraction patterns for the C-YSZ and M-YSZ coatings. The results indicate that both deposited coatings present a tetragonal zirconia structure (t-YSZ) and one cannot detect the monoclinic zirconia or the cubic phase in the coatings. Moreover, the average grain size of the C-YSZ coating was estimated to be between hundreds of nanometers and several microns from the inset SEM image in Fig. 3(c) (which is taken from the edge areas around the pores). By using the Scherrer formula (Ref 20), the average grain size of the M-YSZ coating was calculated to be 20–30 nm.

The transmission electron microscopy image including the lamellar and the lamellar interface zones in the C-YSZ coating is shown in Fig. 6(a). Figure 6(b) shows the enlarged image at a high magnification in the frame of Fig. 6(a), indicating the interface between two adjacent lamellae marked by A and B. The selected area electron diffraction (SAD) patterns taken from the regions in two adjacent parts across the interface marked with A and B in Fig. 6(b) are shown in Fig. 6(c) and (d), respectively. Our careful analysis indicates that both the zones near the interface present the tetragonal lattice structure, which is consistent with the XRD results shown in Fig. (5). As is reported before, this tetragonal phase can be regarded as the predominant metastable phase in all of the plasma-sprayed 8 wt.%Y₂O₃-YSZ coatings (Ref 21–24). In addition to the stable tetragonal lattice structure, one also can see from Fig. 6(b) that the grain size of the C-YSZ coating

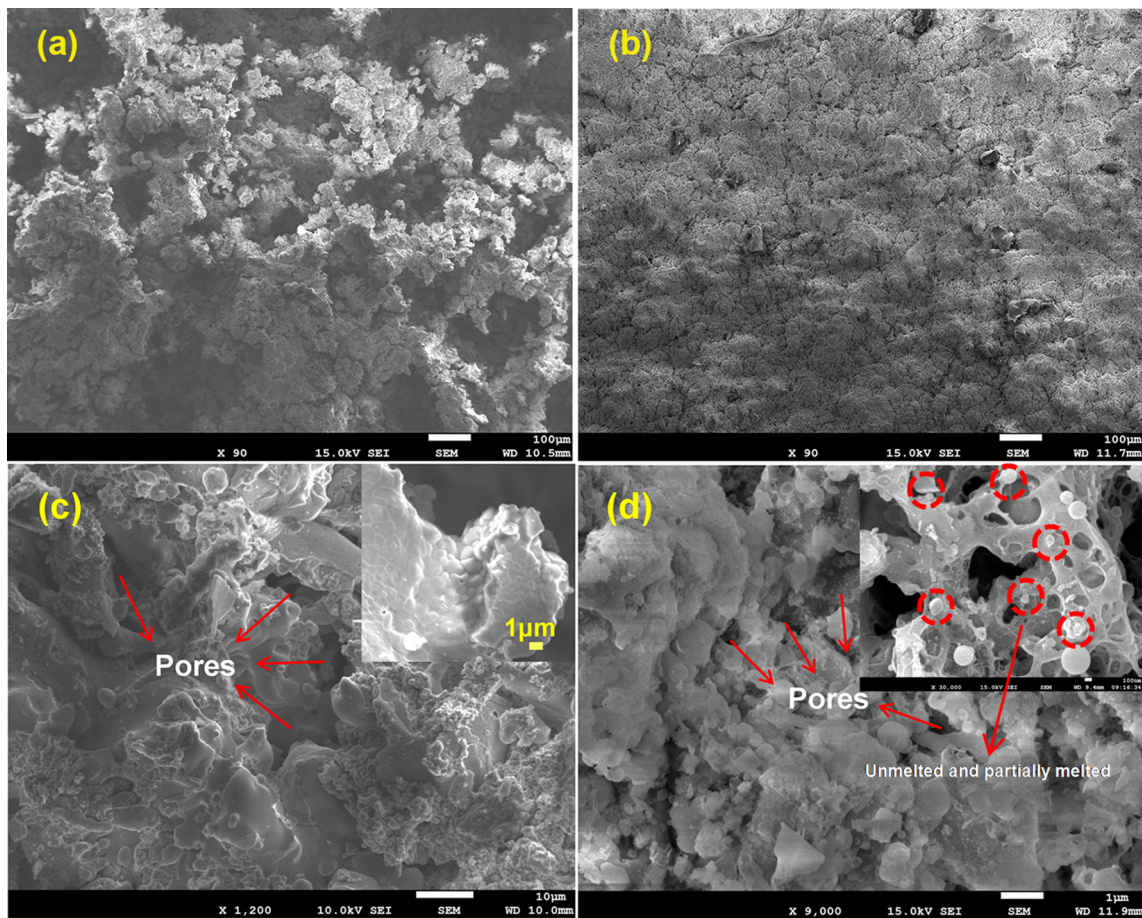
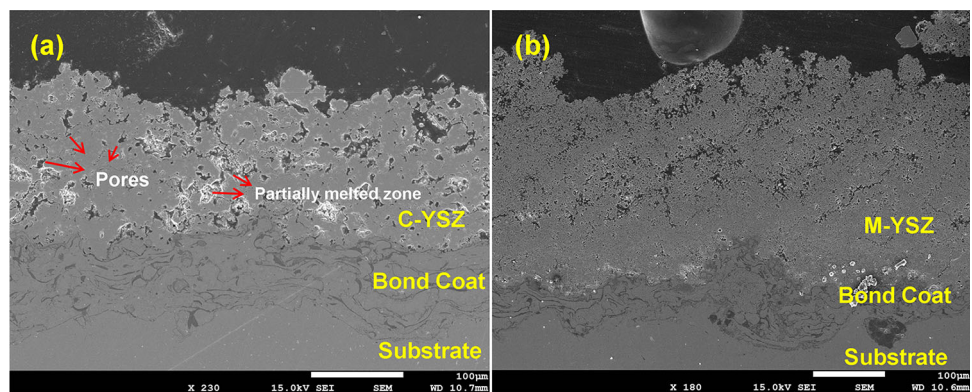


Fig. 3 (a) Surface and (c) enlarged SEM image on surface of C-YSZ. (b) Surface and (d) enlarged SEM image on surface of M-YSZ

Fig. 4 SEM images of the cross sections for (a) C-YSZ and (b) M-YSZ



is larger than 100 nm, which is consistent with the results estimated from Fig. 3(c).

Figure 7(a) displays the transmission electron microscopy image of the M-YSZ abrasible seal coating taken from the relatively thin areas in the coating. By taking into account that M-YSZ was prepared by plasma spraying of a blend of YSZ solution precursor with YSZ nanoparticles, microstructure within grains and at the grain boundaries of the enlarged image in the frame of Fig. 7(a) was further

studied by applying HRTEM and the result is shown in Fig. 7(b). One can see that Fig. 7b shows several neighboring grains of YSZ and the grain boundaries between them can also be clearly detected. First of all, M-YSZ is determined to display tetragonal lattice structure from the SAD patterns shown in the inset of Fig. 7(b). To be better analyzed, neighboring grains are labeled with A and B, while the grain boundary between them is marked with C. The SAD patterns (Fig. 7c) of grain A show the diffraction

with d spacing of 2.994 Å. This value corresponds to (101) tetragonal YSZ plane ($2\theta = 29.83^\circ$ in the XRD results of Fig. 5). As reported before, due to partial stabilization of the zirconia by yttria, cubic phase can be presented in YSZ samples as well as tetragonal phase (Ref 25). However, cubic phase was not detected in region A of Fig. 7(b). Similarly, the structure of grain B (Fig. 7d) also consists of a perfect t-phase lattice and the lattices of region C (Fig. 7e), which is the grain boundary between grains A and B, are tetragonal, whereas there is no sign for the existence of the cubic phase or t'-phase (Ref 26) (formed by a cubic to tetragonal transformation) in the vicinity of grain boundaries or inside the grain boundaries. In comparison with the average grain size of C-YSZ shown in Fig. 6, one can see from Fig. 7 that the average grain size of the M-YSZ coating is much smaller with the size below 30 nm.

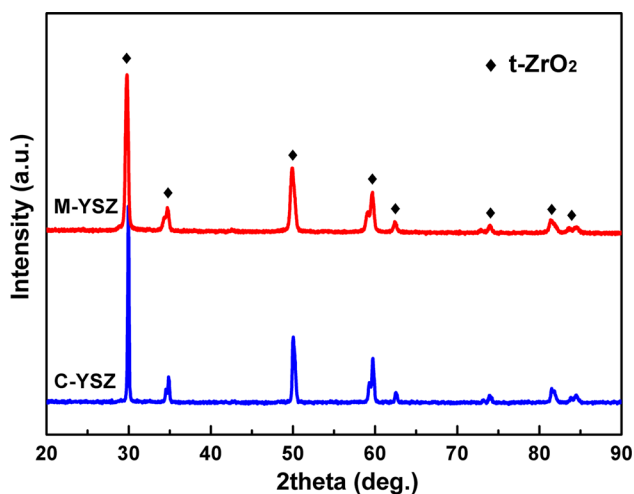


Fig. 5 X-ray diffraction patterns for the deposited C-YSZ and M-YSZ coatings

Mechanical Properties

Figure 8 shows the hardness (HR15Y) and the bond strength of C-YSZ and M-YSZ abrasible seal coatings. Both the hardness and bond strength of the C-YSZ coating are larger than that of the M-YSZ coating. The difference in hardness between C-YSZ (71HR15Y) and M-YSZ (58HR15Y) is caused by the microstructure of the coatings, as discussed in Part 3.1. Although the C-YSZ coating shows a higher porosity and relatively larger pores, the stack of YSZ powders from the molten state makes the coating areas around the pores much denser compared with the M-YSZ coating. Owning a low hardness value, which will definitely benefit the abrasibility of coatings (Ref 27), mainly results from the filling of nanoparticles in M-YSZ in the present work. Figure 8 also shows the bond strength results of C-YSZ and M-YSZ abrasible seal coatings, where one can see that the bond strength of the C-YSZ coating is ~ 15.4 MPa, while for M-YSZ a lower bond strength value of ~ 3.7 MPa is obtained. The bond strength results indicate that adhesion of nanostructured M-YSZ abrasible seal coating is weaker than the C-YSZ abrasible seal coating. This can also be explained by the differences between the microstructures in both coatings. As discussed before, although owning similar porosity, the C-YSZ and M-YSZ abrasible seal coatings show different stack types of YSZ powders from the microstructure point of view. The C-YSZ coating presents the structure of a stack of YSZ powders directly from the molten state, while the M-YSZ coating shows the structure of a stack of melted YSZ nanopowders and unmelted YSZ nanopowders (the inset of Fig. 3d), which will definitely cause different interfacial bonding strengths of YSZ powders and further lead to the variation in bond strength in C-YSZ and M-YSZ. Overall, for the ceramic-based abrasible sealing coatings, usually both the present bond strength values are acceptable. From

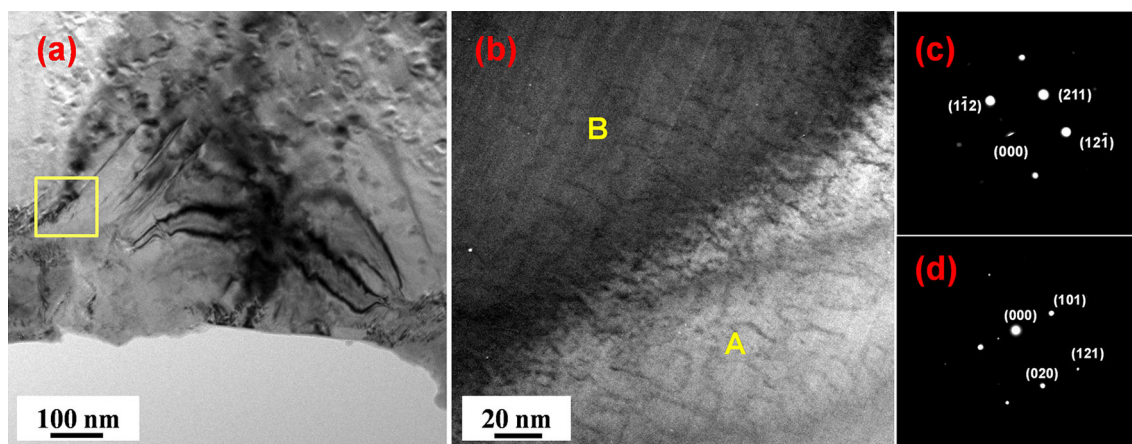


Fig. 6 (a) TEM image of a typical C-YSZ coating. (b) The enlarged view of the frame in (a). (c) and (d) are the SAD patterns corresponding to the regions marked by “A” and “B” in (b), respectively

Fig. 7 (a) TEM image of M-YSZ taken from the relatively thin areas of some YSZ powders. (b) HRTEM image of M-YSZ taken from the frame in (a). (c), (d) and (e) are the SAD patterns corresponding to the regions marked by “A,” “B” and “C” in (b), respectively

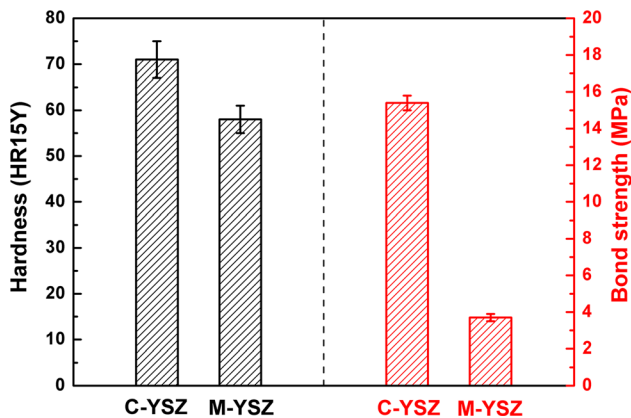
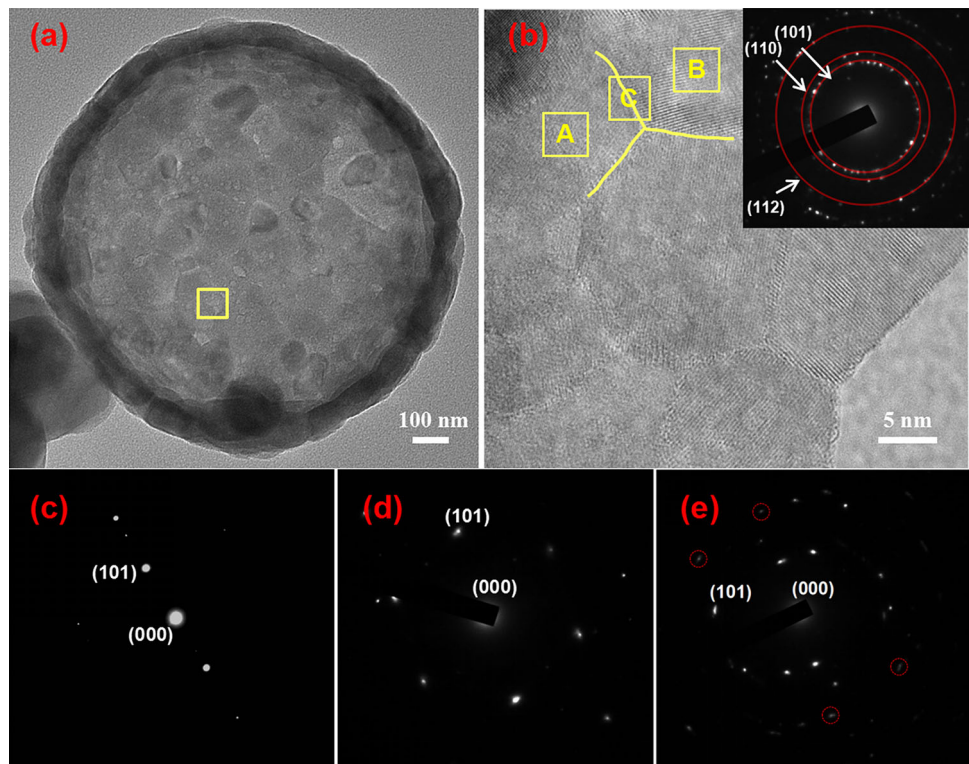


Fig. 8 Comparison of hardness and bond strength for C-YSZ and M-YSZ

the perspective of abrasability, M-YSZ with lower hardness is better in the present work.

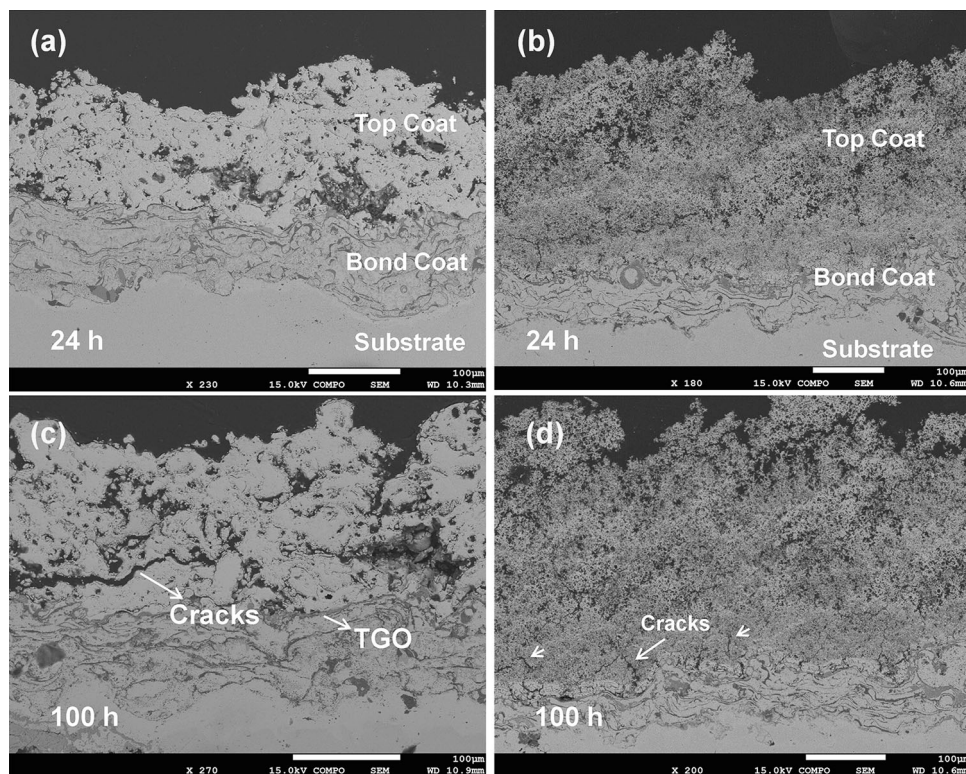
Oxidation Behavior

As is known, the oxidation in the coatings can not only occur through oxygen diffusion from some existing defects such as porosity, cracks and voids but also result from oxygen ions migration behavior by a discrete hopping process through the YSZ lattice (Ref 28). Both the C-YSZ and M-YSZ coatings have high ionic permeability due to

the existing crystal structures (Ref 29). The CoNiCrAlY bonding layer is mainly composed of β and γ phases, in which Y selectively reacts with oxygen due to its high affinity to oxygen. However, its weight percentage in the composition of bonding layer is pretty low, leading to the oxidation of another element aluminum which also has high affinity with oxygen in CoNiCrAlY. As a protective film, the formed Al_2O_3 during oxidation process slows down the rapid oxygen penetration into the bond coat. At the beginning of the oxidation stage, all elements may be oxidized at the interface. After the initial stage, Al_2O_3 grows steadily and continuously (Ref 30).

Cross-sectional SEM microstructures of C-YSZ (Fig. 9a and c) and M-YSZ (Fig. 9b and d) coatings for different oxidation time periods of 24 h and 100 h at 1150 °C are given in Fig. 9, respectively. When the oxidation time is 24 h, the YSZ topcoats of both the C-YSZ and M-YSZ coatings are adherent to the bond coats without any noticeable interfacial oxidation (Fig. 9a and b). When it comes to 100 h, one can see that thin dark oxide scales mainly representing continuous Al_2O_3 layer appear between the YSZ topcoats and the bond coats (Fig. 9c and d). There is a large crack parallel to the coating surface in C-YSZ when the oxidation time is 100 h, while for M-YSZ small cracks perpendicular to the coating surface and small porosity between the YSZ top coat and the bond coat can be detected. Figure 10 is the enlarged views of the cross-sectional SEM microstructures showing the morphology of

Fig. 9 SEM cross-sectional microstructures of oxidized C-YSZ for (a) 24 h and (c) 100 h and M-YSZ for (b) 24 h and (d) 100 h



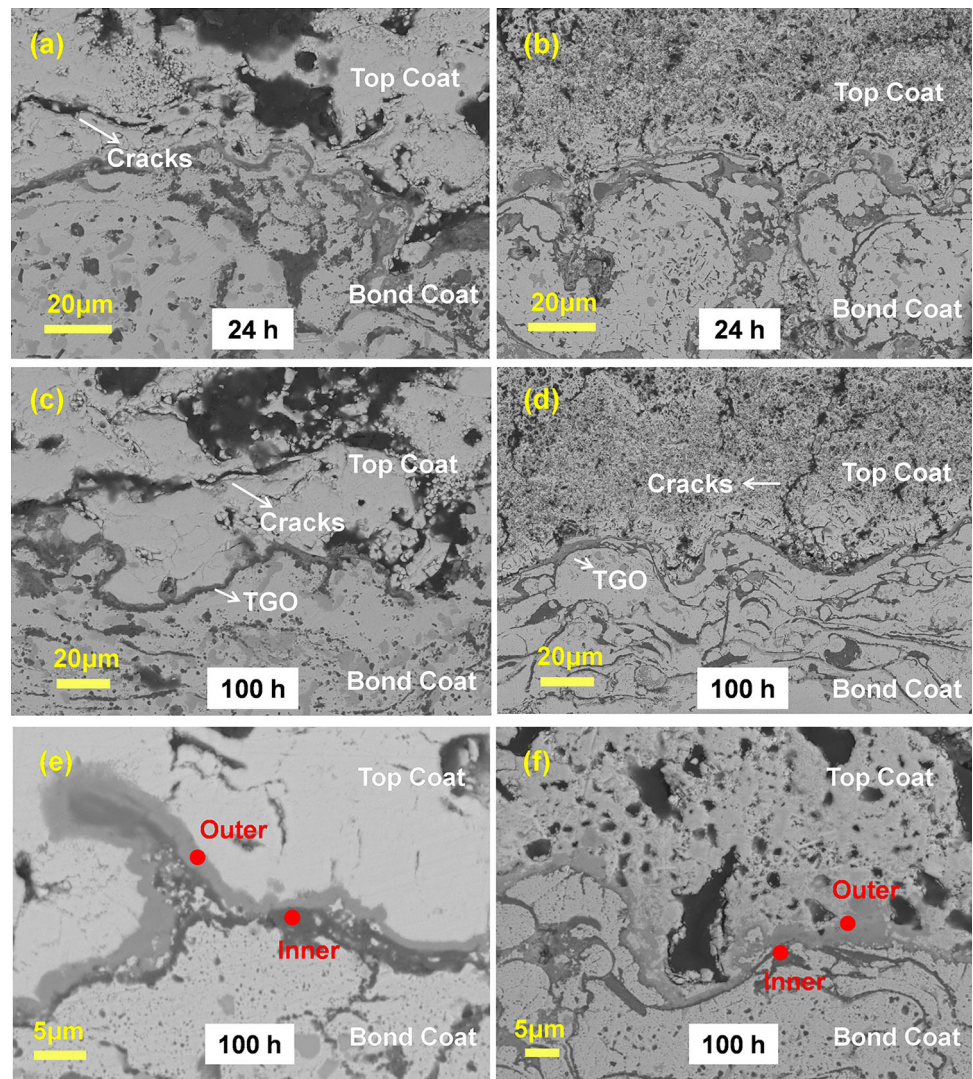
the TGO formed at the interface between the bond coats and the YSZ coats. It can be clearly seen that the TGO shows a one-layer structure in both C-YSZ and M-YSZ coatings after 24-h oxidation test (Fig. 10a, b) and a two-layer structure after 100-h oxidation test (Fig. 10c, d). Our EDS analysis reveals that for the one-layer structure it mainly consists of Y, Al and O (O% = 58, Al% = 29, Y% = 11 and Cr% = 2 in C-YSZ and O% = 55, Al% = 31, Y% = 13 and Cr% = 1 in M-YSZ, at.%). For the two-layer structure, the EDS results show that the inner dark contrast region mainly consists of Al and O (Al% = 38, O% = 57 and Ni% = 5 in C-YSZ and Al% = 34, O% = 60 and Ni% = 6 in M-YSZ, at.%), while the outer gray contrast region mainly contains Y, Al and O (O% = 54, Al % = 31, Y% = 11 and Cr% = 1 in C-YSZ and O% = 49, Al % = 33, Y% = 13 and Cr% = 2 in M-YSZ, at.%). Actually, it is reported that there is a pretty thin outermost porous spinel layer above the outer gray region, which was confirmed to be a spinel structure of NiCr_2O_4 (Ref 31).

From Fig. 10, one can conclude that there are two differences between the C-YSZ and M-YSZ coatings after the oxidation test. One is the uniformity of oxide layers. For C-YSZ, it seems that the thickness of TGO layer is almost uniform for both 24 h and 100 h, while for M-YSZ the TGO layer presents uneven thickness during the oxidation period. The second difference, as observed before, is that after 100-h oxidation test there are large cracks parallel to TGO surface in C-YSZ but instead, small cracks

perpendicular to the coating surface can be detected in M-YSZ. The two differences are mainly ascribed to the different microstructures in both YSZ coatings, as discussed in Part 3.1. For M-YSZ, the special porosity structure with less defects can partly prevent the oxidation through penetration of the oxygen from topcoat to bond coat on the one hand. On the other hand, unlike the conventional YSZ coatings with a large-sized porous microstructure, the nanostructure and submicron size or nanoscale of pore in M-YSZ can slow down the oxygen diffusion from existing defects. Significantly, as is well known, the formation of TGO at the interface of the topcoat and the bond coat causes residual stress. Substantial increase in stress during TGO growth induces spallation of topcoat from bond coat (Ref 32, 33). The uniformly distributed pores with nanosize and submicron size may have improved the stress release ability during the oxidation process (Ref 17). It is reported that the crack structure can be influenced by many factors such as porosity, residual stress, substrate temperature, etc.; the crack formation mechanism for C-YSZ may result from its porous structure, while for M-YSZ the relatively dense structure at inner layer between topcoat and bond coat usually causes vertical cracks (Ref 34–37). By the way, existing voids near the ceramic and intermediate layers in M-YSZ act as a stopper of transverse crack propagation.

Figure 11a displays the x-ray diffraction patterns for C-YSZ and M-YSZ abrasible seal coatings after 120-h

Fig. 10 Enlarged SEM cross-sectional microstructures near the interfaces between the bond coats and the YSZ coats of oxidized C-YSZ for (a) 24 h and (c, e) 100 h and M-YSZ for (b) 24 h and (d, f) 100 h



oxidation test. As can be seen, the M-YSZ coating can always keep a tetragonal zirconia structure and neither of monoclinic zirconia phase or cubic phase could be detected after 120-h oxidation test, indicating an excellent phase stability during the oxidation process. The excellent phase stability mainly originates from the mixed solution precursor plasma spraying method, during which the complete thermal reaction occurs between the coating and most of the nanoparticles with the phase transition from amorphous precursor to tetragonal phase (Ref 18). However, for C-YSZ some new diffraction peaks around (101) come out compared with the XRD result of C-YSZ in Fig. 5, which is determined to be the monoclinic zirconia phase with a low quantity. As is known, the metastable tetragonal phase usually does not transform to the monoclinic phase or the cubic phase until the temperature is higher than 1200 °C. As a result, the phase transition in C-YSZ during oxidation test should be further explored and concluded with firm data. Such a phase transformation behavior has not been

observed in the M-YSZ coatings. This may be because the compressive stresses caused by the increase in the thermal expansion mismatch (Ref 38) are much higher in C-YSZ by conventional plasma-spray technique compared with that of M-YSZ by mixed solution precursor plasma-spray technique, though further deep investigation on the above discussions should be done in the future. The phase transition behavior during the oxidation process may be one of the reasons why large cracks parallel to the C-YSZ coating surface can be observed after 100-h oxidation shown in Fig. 10. Figure 11(b) shows the variation in TGO thickness after 4, 12, 48, 100 and 120 h of oxidation at 1150 °C. First of all, the rate of TGO formation is higher in C-YSZ in comparison with M-YSZ. As can be seen from Fig. 11(b), in the first 12 h of oxidation a rapid increase rate in thickness is observed in C-YSZ and M-YSZ which is due to the high affinity of aluminum with oxygen based on thermodynamics theories (Ref 39). The rate is slowed down until 48 h in both coatings after which the increase is

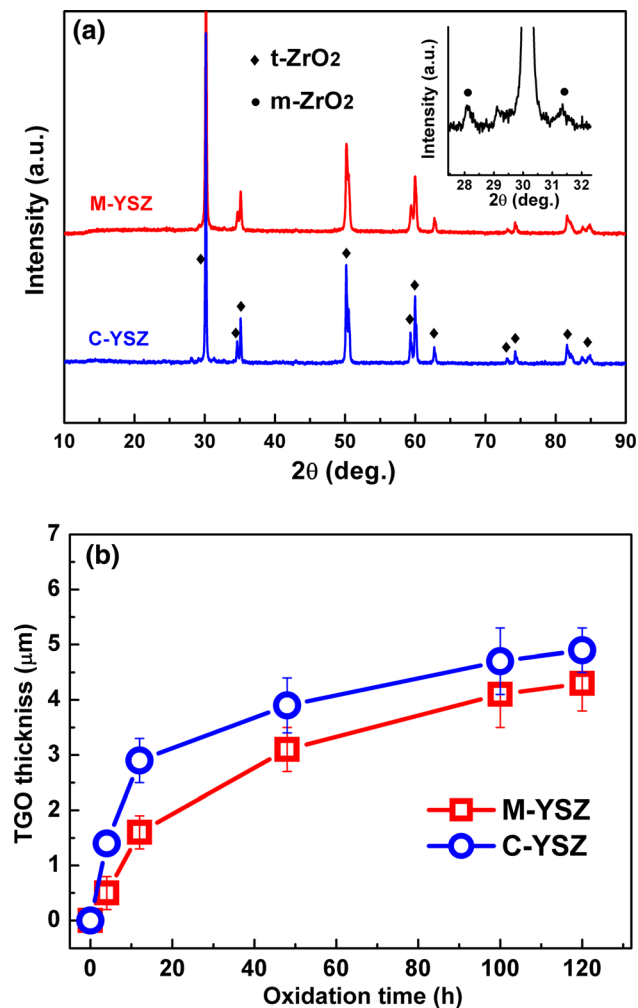


Fig. 11 (a) XRD patterns from the surface of the C-YSZ and M-YSZ coatings after 120-h oxidation test. (b) Changes in TGO layer thickness with oxidation time for the C-YSZ and M-YSZ coatings

slow and reaches a constant rate. The TGO layer growth rate of M-YSZ coating is smaller than that of C-YSZ during the first 16-h oxidation, and then the rate increased considerably so that after 100 h of oxidation reaches to thickest layer. Moreover, the TGO layer thickness after 120-h oxidation is smaller in M-YSZ in comparison with the C-YSZ coating. As mentioned before, the oxygen diffusion into bond coats and the internal oxidation through existence of TGO layer may be from the existence of interconnected porosities, cracks in TGO layer due to its thickening and exerting compressive and bond stresses during thermal cycles and the connection of the porosities from ceramic coating with TGO and CoNiCrAlY layers (Ref 40). The above factors are less severe in M-YSZ compared with that in C-YSZ.

Hence, the nanostructure topcoat in M-YSZ coating may play an important role in decreasing oxygen diffusion into zirconia ceramic layer. It is reported that the formation of a

dense nanostructure and ultrafine grains of YSZ layer plays an effective role in reducing the oxygen permeation within the ceramic zirconia layer (Ref 41). For the abradable seal coatings, the structure cannot be too dense in the whole coatings for both C-YSZ and M-YSZ and the oxygen diffusion may go through microcracks and linked porosities (Ref 42). For C-YSZ, the open and large pores and microcracks can provide easy penetration path for oxygen and result in more oxidation. As indicated from the microstructure of M-YSZ observed in Part. 3.1, the nanostructured M-YSZ has a large number of interfaces of nanomultilayered structure and the grain boundaries and microporosity within the nanostructured coating may further improve its oxidation resistance compared with C-YSZ. As a result, the nanostructure of YSZ in the M-YSZ coatings, to some extent, is preventive for the oxygen access to the coated metal interface.

Hot Corrosion Behavior

Figure 12 shows the surface morphologies of the C-YSZ and M-YSZ coatings after hot corrosion test at 900 °C for 4 h. After 4-h hot corrosion test, some spallation can be observed in both coatings in Fig. 12(a, b) compared with Fig. 3. It can be seen from Fig. 12(c, d) that many crystals with rod shape are deposited on the surface of both the C-YSZ and M-YSZ coatings. The results of EDS analysis of the boxes in Fig. 12(c, d) show that the regions mainly contain O, V and Y (O% = 51 at.%, V% = 23 at.%, Y% = 23 at.%, Zr% = 3 at.% for C-YSZ in Fig. 12(c) and O% = 53 at.%, V% = 26 at.%, Y% = 20 at.%, Zr% = 1 at.% for M-YSZ in Fig. 12(d)). Moreover, the large peeling vacancies as well as some large transverse cracks appeared in the C-YSZ coating, while some large vertical or oblique cracks were found in the M-YSZ coating as shown in Fig. 12e, f. Significantly, after 4-h hot corrosion test, degradation of the C-YSZ coating occurred at the ceramic–bond coat interface, while for the M-YSZ coating the ceramic–bond coat interface did not result in serious degradation.

The mechanisms on the appearance of these crystals on the surface of both C-YSZ and M-YSZ coatings have been described in some previous works (Ref 43, 44). Firstly, the molten salts penetrate into the coatings through the pores and microcracks which are usually formed in the plasma spray coatings. After that, the NaVO₃ can be formed from the reactions between corrosive salts, which can further react with stabilizer of ZrO₂(Y₂O₃):

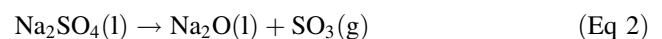
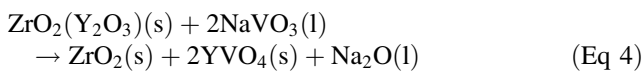
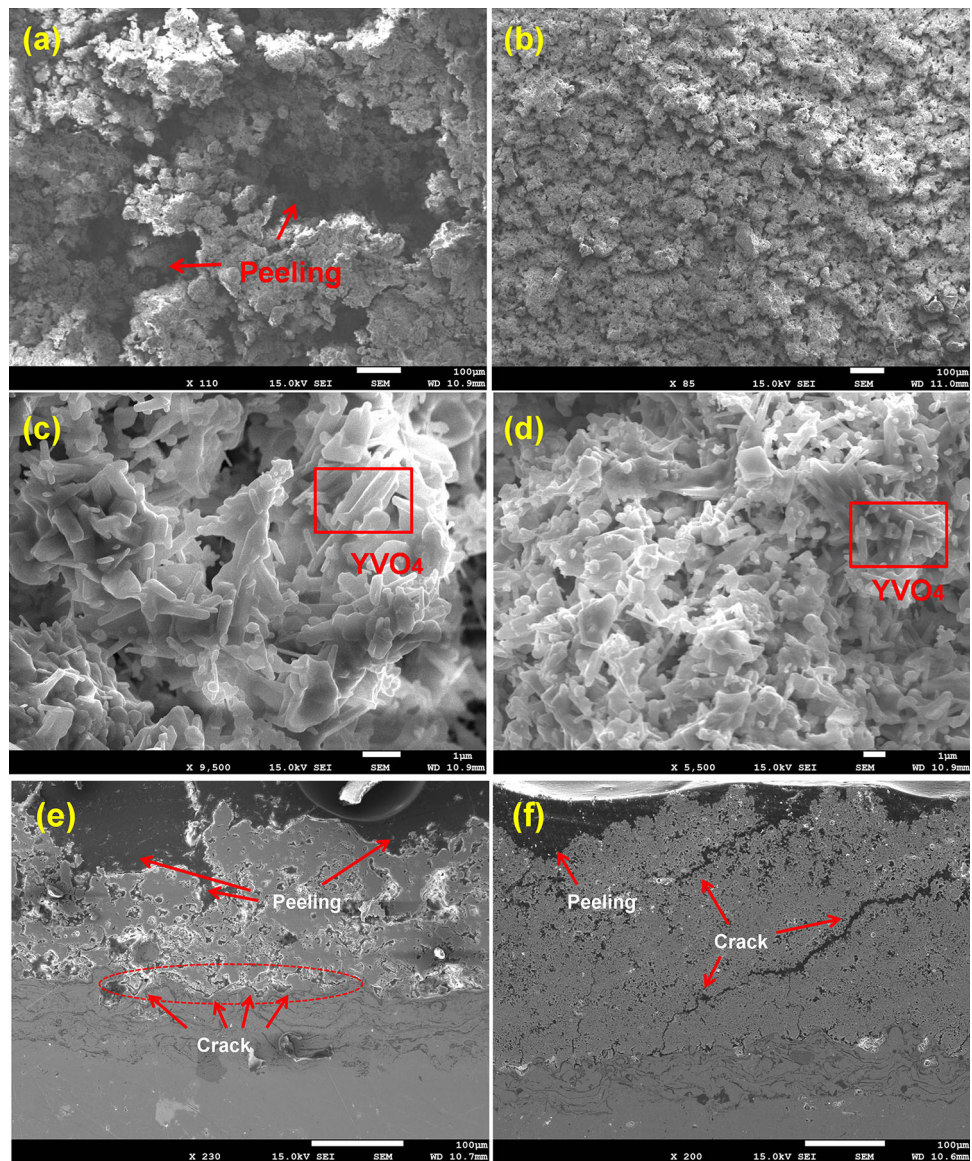


Fig. 12 SEM images after 4-h corrosion test for C-YSZ: (a) the surface, (c) the enlarged view of surface and (e) the cross section and for M-YSZ: (b) the surface, (d) the enlarged view of surface and (f) the cross section



Finally, the formation of YVO_4 crystals is done when the Y_2O_3 is totally depleted from YSZ, leading to the transformation of tetragonal to monoclinic ZrO_2 . This phase transformation behavior can result in volume changes, causing further cracks during the high-temperature thermal cycling process, as shown in Fig. 12(e) and (f). As a result, the amount of YVO_4 crystals and the monoclinic phase is usually used as an evaluation method for the hot corrosion progress and resistance (Ref 44, 45). In the present work, comparing the corrosion resistance between C-YSZ and M-YSZ can be further done by comparing the volume percents of the monoclinic ZrO_2 phase in both coatings:

$$m\% = (m_1 + m_2) / (t + m_1 + m_2) \quad (\text{Eq 5})$$

where t is the peak intensity of tetragonal ZrO_2 from the (101) plane, and m_1 and m_2 are the peak intensities of monoclinic ZrO_2 from the $(\bar{1}11)$ and (111) planes, and they can all be obtained from Fig. 13(a). From Eq (5), it can be calculated that the amounts of monoclinic phase in C-YSZ and M-YSZ are $\sim 48\%$ and $\sim 31\%$. So for the C-YSZ coating the volume percent of monoclinic ZrO_2 is higher than that of the M-YSZ coating in the early stage during the hot corrosion test.

Figure 13(a) shows the XRD results for the C-YSZ and M-YSZ coatings after 24-hour corrosion test. In addition to tetragonal ZrO_2 which is the predominant phase in both coatings, diffraction peaks corresponding to monoclinic ZrO_2 and tetragonal YVO_4 phases resulting from the

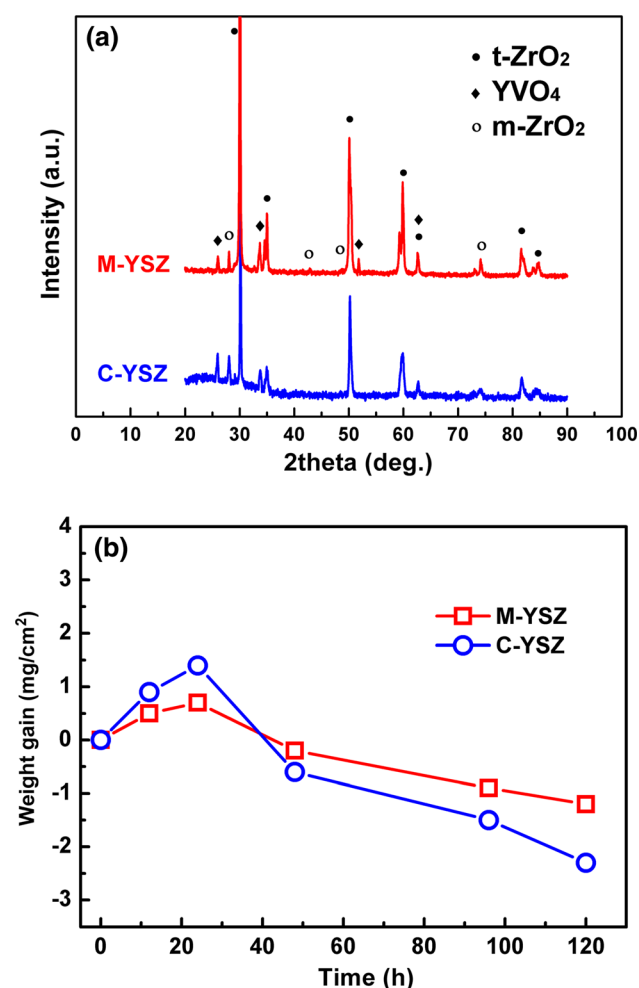


Fig. 13 (a) XRD results for the C-YSZ and M-YSZ coatings after 24-hour corrosion test; (b) mass change per unit area versus hot corrosion time for C-YSZ and M-YSZ after hot corrosion at 900 °C

corrosion process can also be obtained. Figure 13(b) shows the hot corrosion kinetics (mass change per unit area) of the C-YSZ and M-YSZ coatings coated with mixed salts at 900 °C. It is seen that for both coatings the weight change is above zero before ~40 h and then large mass loss is due to the severe scale spallation during the corrosion exposure and cooling stages, leading to the weight change down below zero as shown in Fig. 13(b). In comparison, one can see from Fig. 13(b) that the M-YSZ coating seems to present better hot corrosion resistance in the early stage compared with that of C-YSZ because the mass decrease was lower. One should notice that the weight change is above zero after 4-h hot corrosion test from Fig. 13(b), which may contradict the SEM observations in Fig. (12). This may be caused by the loss of loose products on the surface during the samples' preparation process for the cross-sectional observation. Overall, both the C-YSZ and M-YSZ abrasible seal coatings fail to display excellent hot corrosion resistance in the present work, which may be

caused by the abrasible seal coatings' own special characteristics. It is reported that the YSZ/alumina composite coatings present higher hot corrosion resistance than the YSZ coating (Ref 45, 46), giving some ideas on designing M-YSZ/Al abrasible seal coatings with better hot corrosion resistance in the future.

Conclusions

In this study, two kinds of abrasible seal coatings were successfully prepared by applying the conventional plasma spraying method with improved nanostructured powders and by mixed solution precursor plasma spraying technique. A detailed study of the microstructure and mechanical properties was made between the C-YSZ and M-YSZ coatings, and the results showed that the size of existing pores is much larger and the melted particles distributed around the pores are much denser in C-YSZ presenting higher hardness and bond strength compared with that of M-YSZ presenting lower hardness and smaller bond strength. Moreover, the stability of the C-YSZ coating and analysis from the microstructure point of view were compared to the particulate M-YSZ coating by means of high-temperature oxidation and hot corrosion test. The M-YSZ coatings display better oxidation resistance due to the nanostructure topcoat compared with C-YSZ. However, both the C-YSZ and M-YSZ abrasible seal coatings did not present excellent hot corrosion resistance during long-time hot corrosion process. This work may shed light on the design of nanostructured abrasible seal coatings.

Acknowledgements We gratefully acknowledge support from the National Key Research and Development Program of China (No. 2018YFC1902401) and the National Natural Science Foundation of China (No. 51671180). This work is also supported by Key Deployment Projects of the Chinese Academy of Sciences (ZDRW-CN-2019-01) and Projects of the Innovation Academy for Green Manufacture, Chinese Academy of Sciences (IAGM 2020DB04, IAGM 2020C22).

References

1. D. Sporer, S. Wilson, I. Giovannetti, A. Refke, and M. Giannozzi, On the Potential of Metal and Ceramic Based Abradables in Turbine Seal Applications, *Proceedings of the thirty-sixth turbomachinery symposium.*, 2007, p 79-86
2. T. Steinke, G. Mauer, R. Vaßen, D. Stöver, D. Roth-Fagaraseanu and M. Hancock, Process Design and Monitoring for Plasma-sprayed Abradable Coatings, *J. Therm. Spray Technol.*, 2010, **19**(4), p 756–764.
3. E. Irissou, A. Dadouche and R.S. Lima, Tribological Characterization of Plasma-sprayed CoNiCrAlY-BN Abradable Coatings, *J. Therm. Spray Technol.*, 2014, **23**(1–2), p 252–261.
4. M.H. Foroushani, M. Shamanian, M. Salehi and F. Davar, Porosity Analysis and Oxidation Behavior of Plasma Sprayed

- YSZ and YSZ/LaPO₄ Abradable Thermal Barrier Coatings, *Ceram. Int.*, 2016, **42**(14), p 15868–15875.
5. K.Y. Ding, T.T. Cheng and Z.Y. Han, Formation and Properties of Porous ZrO₂-8wt%Y₂O₃ Coatings, *Rare Metal Mat. Eng.*, 2018, **47**(6), p 1677–1681.
 6. S. Ebert, R. Mücke, D. Mack, R. Vaßen, D. Stöver, T. Wobst and S. Gebhard, Failure Mechanisms of Magnesia Alumina Spinel Abradable Coatings under Thermal Cyclic Loading, *J. Eur. Ceram. Soc.*, 2013, **33**(15–16), p 3335–3343.
 7. R. Vaßen, A. Stuke and D. Stöver, Recent Developments in the Field of Thermal Barrier Coatings, *J. Therm. Spray Technol.*, 2009, **18**(2), p 181–186.
 8. D. Stöver, G. Pracht, H. Lehmann, M. Dietrich, J.E. Döring and R. Vaßen, New Material Concepts for the Next Generation of Plasma-sprayed Thermal Barrier Coatings, *J. Therm. Spray Technol.*, 2004, **13**(1), p 76–83.
 9. B. Saruhan, P. Francois, K. Fritscher and U. Schulz, EB-PVD Processing of Pyrochlore-structured La₂Zr₂O₇-based TBCs, *Surf. Coat. Technol.*, 2004, **182**(2–3), p 175–183.
 10. X. Chen, X. Cao, B. Zou, J. Gong and C. Sun, Corrosion of Lanthanum Magnesiumhex-aluminate as Plasma-sprayed Coating and as Bulk Material When Exposed to Molten V₂O₅-containing Salt, *Corros. Sci.*, 2015, **91**, p 185–194.
 11. H.D. Steffens and R. Kaczmarek, Thermal Barrier Coatings for Heat Engines, *Weld. World*, 1990, **28**(11–12), p 224–230.
 12. M. Saremi, A. Afrasiabi and A. Kobayashi, Microstructural Analysis of YSZ and YSZ/Al₂O₃ Plasma Sprayed Thermal Barrier Coatings after High Temperature Oxidation, *Surf. Coat. Technol.*, 2008, **202**(14), p 3233–3238.
 13. J. Gang, J.P. Morniroli and T. Grosdidier, Nanostructures in Thermal Spray Coatings, *Scr. Mater.*, 2003, **48**(12), p 1599–1604.
 14. M. Gell, Application Opportunities for Nanostructured Materials and Coatings, *Mater. Sci. Eng. A*, 1995, **204**(1–2), p 246–251.
 15. H. Chen and C.X. Ding, Nanostructured Zirconia Coating Prepared by Atmospheric Plasma Spraying, *Surf. Coat. Technol.*, 2002, **150**(1), p 31–36.
 16. J.F. Li, H. Liao, X.Y. Wang, B. Normand, V. Ji, C.X. Ding and C. Coddet, Improvement in Wear Resistance of Plasma Sprayed Yttria Stabilized Zirconia Coating Using Nanostructured Powder, *Tribol. Int.*, 2004, **37**(1), p 77–84.
 17. X.M. Sun, L.Z. Du, H. Lan, H.F. Zhang, R.Y. Liu, Z.G. Wang, S.G. Fang, C.B. Huang, Z.A. Liu and W.G. Zhang, Study on Thermal Shock Behavior of YSZ Abradable Sealing Coating Prepared by Mixed Solution Precursor Plasma Spraying, *Surf. Coat. Technol.*, 2020, **397**, p 126045.
 18. Z. Wang, L.Z. Du, H. Lan, C.B. Huang and W.G. Zhang, Preparation and Characterization of YSZ Abradable Sealing Coating Through Mixed Solution Precursor Plasma Spraying, *Ceram. Int.*, 2019, **45**(9), p 118023–211811.
 19. L.Z. Du, W.T. Zhang, W.G. Zhang, T.T. Zhang, H. Lan and C.B. Huang, Tribological and Oxidation Behaviors of the Plasma Sprayed NiCoCrAlY-Cr₂O₃-AgVO₃ Coating, *Surf. Coat. Technol.*, 2016, **298**, p 7–14.
 20. Y. Zhao and Y. Gao, Deposition of Nanostructured YSZ Coating from Spray-dried Particles with No Heat Treatment, *Appl. Surf. Sci.*, 2015, **346**, p 406–414.
 21. J. Moon, H. Choi, H. Kim and C. Lee, The effects of Heat Treatment on the Phase Transformation Behavior of Plasma-sprayed Stabilized ZrO₂ Coatings, *Surf. Coat. Technol.*, 2002, **155**(1), p 1–10.
 22. M. Leoni, R.L. Jones and P. Scardi, Phase Stability of Scandia-yttria-stabilized Zirconia TBCs, *Surf. Coat. Technol.*, 1998, **108–109**, p 107–113.
 23. G.-J. Yang, Z.-L. Chen, C.-X. Li and C.-J. Li, Microstructural and Mechanical Property Evolutions of Plasma-sprayed YSZ Coating during High-temperature Exposure: Comparison Study between 8YSZ and 20YSZ, *J. Therm. Spray Technol.*, 2013, **22**(8), p 1294–1302.
 24. Y.Y. Chen and W.C.J. Wei, Processing and Characterization of Ultra-thin Yttria-stabilized zirconia (YSZ) Electrolytic Films for SOFC, *Solid State Ionics*, 2006, **177**(3–4), p 351–357.
 25. S. Nazarpour, C. López-Gándara, F.M. Ramos and A. Cirera, Phase Transformation Studies on YSZ Doped with Alumina. Part 1: Metastable phases, *J. Alloy. Compd.*, 2010, **505**(2), p 527–533.
 26. M. Yashima, M. Kakihana, and M. Yoshimura, Metastable Phase Diagrams in the Zirconia-containing Systems Utilized in Solid-oxide Fuel Cell Application, *Solid State Ionics*, 1996, **86–88**(2), p 1131
 27. M.Z. Yi, J.W. He, B.Y. Huang and H.J. Zhou, Friction and Wear Behaviour and Abradability of Abradable Seal Coating, *Wear*, 1999, **231**(1), p 47–53.
 28. N. Narimanin and M. Saremi, A Study on the Oxidation Resistance of Electrodeposited and Nanostructured YSZ Thermal Barrier Ceramic Coatings, *Ceram. Int.*, 2015, **41**(10), p 13810–13816.
 29. G. Di Girolamo and L. Pagnotta, Thermally Sprayed Coatings for High-temperature Applications, *Recent Pat. Mater. Sci.*, 2011, **4**(3), p 173–190.
 30. F. Tang, L. Ajdelsztajn and J.M. Schoenung, Influence of Cryomilling on the Morphology and Composition of the Oxide Scales Formed on HVOF CoNiCrAlY Coatings, *Oxid. Met.*, 2004, **61**(3), p 219–238.
 31. Y. Hua, C.Y. Cai, Y.G. Wang, H.C. Yu, Y.C. Zhou and G.W. Zhou, YSZ/NiCrAlY Interface Oxidation of APS Thermal Barrier Coatings, *Corros. Sci.*, 2018, **142**, p 22–30.
 32. F. Traeger, M. Ahrens, R. Vaßen and D. Stöver, A Life Time Model for Ceramic Thermal Barrier Coatings, *Mater. Sci. Eng. A*, 2003, **358**(1–2), p 255–265.
 33. A.G. Evans, D. Mumm, J. Hutchinson, G. Meier and F. Pettit, Mechanisms Controlling the Durability of Thermal Barrier Coatings, *Prog. Mater. Sci.*, 2001, **46**(5), p 505–553.
 34. S. Sampath, X.Y. Jiang, J. Matejcek, A.C. Leger and A. Vardelle, Substrate Temperature Effects on Splat Formation, Microstructure Development and Properties of Plasma Sprayed Coatings Part I: Case Study for Partially Stabilized Zirconia, *Mater. Sci. Eng. A*, 1999, **272**, p 181–188.
 35. A. Kulkarni, A. Vaidya, A. Goland, S. Sampath and H. Herman, Processing Effects on Porosity-Property Correlations in Plasma Sprayed Yttria-Stabilized Zirconia Coatings, *Mater. Sci. Eng. A*, 2003, **359**, p 100–111.
 36. S. Sampath, U. Schulz, M.O. Jarligo and S. Kuroda, Processing Science of Advanced Thermal-Barrier Systems, *MRS Bull.*, 2012, **37**(10), p 903–910.
 37. V. Viswanathan, G. Dwivedi and S. Sampath, Engineered Multilayer Thermal Barrier Coatings for Enhanced Durability and Functional Performance, *J. Am. Ceram. Soc.*, 2014, **97**(9), p 2770–2778.
 38. P.L. Ke, Y.N. Wu, Q.M. Wang, J. Gong, C. Sun and L.S. Wen, Study on Thermal Barrier Coatings Deposited by Detonation Gun Spraying, *Surf. Coat. Technol.*, 2005, **200**(7), p 2271–2276.
 39. A. Keyvani, M. Saremi and M.H. Sohi, Oxidation Resistance of YSZ-alumina Composites Compared to Normal YSZ TBC Coatings at 1100 °C, *J. Alloys Compd.*, 2011, **509**(33), p 8370–8377.
 40. A.C. Fox and T.W. Clyne, Oxygen Transport by Gas Permeation Through the Zirconia Layer in Plasma Sprayed Thermal Barrier Coatings, *Surf. Coat. Technol.*, 2004, **184**(2–3), p 311–321.
 41. C. Zhou, N. Wang and H. Xu, Comparison of Thermal Cycling Behavior of Plasma-sprayed Nanostructured and Traditional Thermal Barrier Coatings, *Mater. Sci. Eng. A*, 2006, **452–453**, p 569–574.

42. A. Keyvani, M. Saremi, M. Heydarzadeh Sohi, and Z. Valefi, A Comparison on Thermomechanical Properties of Plasma-sprayed Conventional and Nanostructured YSZ TBC Coatings in Thermal Cycling, *J. Alloy. Compd.*, 2012, **541**, p 488-494
43. R.L. Jones, Some Aspects of the Hot Corrosion of Thermal Barrier Coatings, *J. Therm. Spray Technol.*, 1997, **6**(1), p 77–84.
44. I. Gurrappa and A. Sambasiva Rao, Thermal Barrier Coatings for Enhanced Efficiency of Gas Turbine Engines, *Surf. Coat. Technol.*, 2006, **201**(6), p 3016-3029
45. M. Saremi, Z. Valefi and N. Abaeian, Hot Corrosion, High Temperature Oxidation and Thermal Shock Behavior of Nanoagglomerated YSZ-Alumina Composite Coatings Produced by Plasma Spray Method, *Surf. Coat. Technol.*, 2013, **221**, p 133–141.
46. A. Keyvani, Microstructural Stability Oxidation and Hot Corrosion Resistance of Nanostructured $\text{Al}_2\text{O}_3/\text{YSZ}$ Composite Compared to Conventional YSZ TBC Coatings, *J. Alloy. Compd.*, 2015, **623**, p 229–237.

Publisher's Note Springer Nature remains neutral with regard to jurisdictional claims in published maps and institutional affiliations.